Bloch Wavefunction Reconstruction using Multidimensional Photoemission Spectroscopy

Michael Schüler,[1,*] Tommaso Pincelli,[2] Shuo Dong,[2] Thomas P. Devereaux,[1,3]
Martin Wolf,[2] Laurenz Rettig,[2] Ralph Ernstorfer,[2,†] and Samuel Beaulieu[2,4,‡]

[1]*Stanford Institute for Materials and Energy Sciences (SIMES), SLAC National Accelerator Laboratory, Menlo Park, CA 94025, USA*
[2]*Fritz Haber Institute of the Max Planck Society, Faradayweg 4-6, 14195 Berlin, Germany*
[3]*Department of Materials Science and Engineering, Stanford University, Stanford, California 94305, USA*
[4]*Université de Bordeaux - CNRS - CEA, CELIA, UMR5107, F33405, Talence, France*

Angle-resolved spectroscopy is the most powerful technique to investigate the electronic band structure of crystalline solids. To completely characterize the electronic structure of topological materials, one needs to go beyond band structure mapping and probe the texture of the Bloch wavefunction in momentum-space, associated with Berry curvature and topological invariants. Because phase information is lost in the process of measuring photoemission intensities, retrieving the complex-valued Bloch wavefunction from photoemission data has yet remained elusive. In this Article, we introduce a novel measurement methodology and observable in extreme ultraviolet angle-resolved photoemission spectroscopy, based on continuous modulation of the ionizing radiation polarization axis. By tracking the energy- and momentum-resolved amplitude and phase of the photoemission modulation upon polarization variation, we reconstruct the Bloch wavefunction of prototypical semiconducting transition metal dichalcogenide 2H-WSe_2 with minimal theory input. This novel experimental scheme, which is articulated around the manipulation of the photoionization transition dipole matrix element, in combination with a simple tight-binding theory, is general and can be extended to provide insights into the Bloch wavefunction of many relevant crystalline solids.

INTRODUCTION

Wavefunctions are mathematical descriptions of the quantum state of a system and are ubiquitous in quantum mechanics. They are complex-valued probability amplitudes, and the probabilities for the results of any measurements made on a quantum system can be derived from them. Because of their complex-valued nature, and since most experimental techniques are sensitive to the square-modulus of the wavefunction – leading to a loss of the phase information – reconstructing wavefunctions from experimental observables is a challenging task.

The use of interferometric measurement techniques, which use the interference pattern generated by superimposed waves to extract their relative phases, has been used to experimentally reconstruct the electronic wavefunction of atoms and molecules. For example, the interferometric nature of the photoelectric effect, as well as its time-reversed analog *photorecombination*, have been used to reconstructed the orbitals of atoms [1, 2], aligned gas-phase molecules [3, 4], as well as molecular adsorbates [5, 6]. Real-space excitonic wavefunction has also recently reconstruct using the Fourier transform of the momentum-space photoemission intensity [7, 8], assuming a flat phase.

Knowledge about the electronic band structure, *i.e.* the momentum-dependent energy eigenvalues, and the associated Bloch wavefunction are essential to understand the transport, optical and magnetic properties of crystalline solids. With the discovery of topological materials [9], it became clear that accessing knowledge beyond band structure is of fundamental importance to understand the unique properties of this novel class of quantum materials. The topologically nontrivial nature of materials emerges from the winding of the phase of their Bloch wavefunctions in momentum-space, associated with Berry curvature [10] and topological invariants, *e.g.* Chern numbers. Reconstructing the band structure and the associated amplitude and phase of the Bloch wavefunction is thus of capital importance to fully characterized the electronic structure of (topological) materials.

While the electronic band structures of crystalline materials can be mapped using angle-resolved photoemission spectroscopy (ARPES) [11], reconstructing the associated Bloch wavefunction is still a great challenge. Whereas complex-valued information about the Bloch wavefunction of electrons inside solids is encoded in the photoionization transition dipole matrix element underlying the photoelectric effect, leading to subtle anisotropic modulation of the signal in momentum-energy space, a general route to reconstruct the Bloch wavefunction from photoemission data have not been established yet.

Circular dichroism in the photoelectron angular distribution (CDAD) is a powerful quantity that can be used to probe *e.g.* electronic chirality in graphene [12], helical spin textures in topological insulators [13], the orbital Rashba effect in metals [14] and the Berry curvature in TMDCs [15–18]. By contrast, linear dichroism in the photoelectron angular distribution (LDAD) is typically assumed to encode the non-relativistic symmetry of the wavefunction [19–22], but does not contain enough information to access the phase of the Bloch wavefunction.

In this Article, we introduce a novel measurement scheme in multidimensional photoemission spectroscopy allowing to completely reconstruct the complex-valued Bloch wavefunction. Indeed, tracking the energy- and momentum-resolved

* schuelem@stanford.edu
† ernstorfer@fhi-berlin.mpg.de
‡ samuel.beaulieu@u-bordeaux.fr

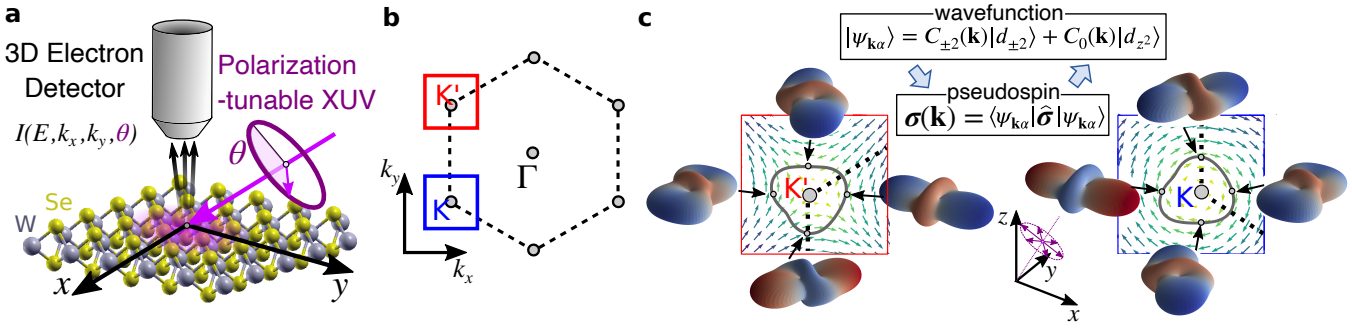

FIG. 1. **Experimental setup:** **(a)** Experimental scheme of the polarization-modulated photoemission. A polarization-axis-tunable linearly polarized femtosecond XUV pulse (21.7 eV) is focused onto a bulk 2H-WSe_2 crystal at an angle of incidence of 65° with respect to the surface normal, ejecting photoelectrons which are detected by a time-of-flight momentum microscope, allowing to measure the energy- and momentum-resolved photoemission intensity as a function of the polarization axis angle θ. **(b)** Sketch of the first Brillouin zone. **(c)** Bloch wavefunction of the top valence band of monolayer WSe_2 (projected onto the W atom) at selected momentum points close to the K and K′ (corresponding to the boxes in **b**) valley. The coordinate system indicates the spatial orientation in real space. Close to the K/K′ valley the Bloch wavefunction is composed of $|d_{\pm2}\rangle$ and $|d_{z^2}\rangle$ orbitals with corresponding coefficients. There is a one-to-one map of the complex wavefunction coefficients $C_{0,\pm2}(\mathbf{k})$ to the orbital pseudospin $\boldsymbol{\sigma}(\mathbf{k})$; the corresponding texture is represented by the vector field. The gray thick is a contour of maximum photoemission intensity for a typical binding energy.

modulation of the photoemission intensity upon continuous rotation of the ionizing radiation polarization axis, complemented by minimal theory input enable us to fully reconstruct the Bloch wavefunction underlying the electronic band structure of crystalline solids.

For the first demonstration of our novel approach, we choose to study the layered transition metal dichalcogenide (TMDC) 2H-WSe_2. Despite its inversion-symmetric crystal structure, this material possesses locally broken inversion symmetry within each layer and strong spin-orbit coupling, leading to entangled layer, spin, orbital, and valley degrees of freedom [23]. The topmost layer surface sensitivity of extreme ultraviolet (XUV)-ARPES allows to directly probe this intricate hidden spin [15, 24] and orbital [25] texture. This peculiar spin-orbital-valley locking leads to optical selection rules allowing for the generation of spin- and valley-polarized excited carriers [26], to orbital Hall effect (OHE) [27], and the emergence of orbital Hall insulating phases [28]. The valley-dependent orbital pseudospin texture is also at the origin of the emergence of local Berry curvature [10], associated with the winding of the wavefunction phase in momentum-space. Such material is thus well suited to test our novel polarization-resolved multidimensional photoemission spectroscopy approach.

RESULTS

The momentum-dependence of photoemission spectra contains rich information on the band structure, but, as only the intensity is measured, the loss of phase information renders a reconstruction of the Bloch wavefunction difficult. We rise to such a challenge by increasing the dimensionality of the measurement: photoemission intensity is recorded while continuously varying the polarization axis direction of linearly polarized XUV ionizing radiation (characterized by the angle θ). By looking at the energy- and momentum-resolved modulation of the photoemission intensity upon polarization rotation, we can access the orientation of hybridized orbitals involved in the photoemission process, allowing us to retrieve the orbitals' relative phase information. To this end, we use our multidimensional photoemission setup featuring a home-built high-repetition-rate (500 kHz) femtosecond XUV source (polarization-tunable) coupled to a time-of-flight momentum microscope [29, 30] (see Fig. 1a and Methods). Measuring the photoemission intensity resolved in energy (E) and both parallel momenta (k_x, k_y) for each polarization axis direction (θ) yields four-dimensional data sets $I(E, k_x, k_y, \theta)$. While the multidimensional photoemission data for each polarization direction naturally includes linear dichroism, the photoemission intensity modulation upon continuous rotation of θ, gives qualitatively new information about the participating orbitals, as detailed below.

The photoemission processes can be described by Fermi's golden rule,

$$I(E,\mathbf{k},\theta) \propto \left|\langle \mathbf{k}, E|\mathbf{e}(\theta)\cdot\hat{\mathbf{r}}|\psi_{\mathbf{k}\alpha}\rangle\right|^2 \delta(\varepsilon_{\mathbf{k}\alpha}+\hbar\omega-E)\,, \quad (1)$$

where $|\psi_{\mathbf{k}\alpha}\rangle$ is the initial Bloch state with energy $\varepsilon_{\mathbf{k}\alpha}$, $\mathbf{e}(\theta)$ the polarization vector of the photons (energy $\hbar\omega$), $\hat{\mathbf{r}}$ the dipole operator, and $|\mathbf{k}, E\rangle$ the final states. At fixed in-plane momentum $\mathbf{k} = (k_x, k_y)$ and photoelectron energy E, the magnitude of the photoemission intensity is fully determined by the dipole matrix element $M(E,\mathbf{k},\theta) = \langle \mathbf{k}, E|\mathbf{e}(\theta)\cdot\hat{\mathbf{r}}|\psi_{\mathbf{k}\alpha}\rangle$ for the band index α. Its value is determined by (i) the direction of the photoelectron $\mathbf{p} = (k_x, k_y, k_\perp)$, (ii) the light polarization $\mathbf{e}(\theta)$, and (iii) the orbital character and orientation of the initial state. In particular, the relative orientation of $\mathbf{e}(\theta)$ and $\mathbf{p}$ matters: $I(E,\mathbf{k},\theta)$ is generally enhanced if their are parallel, and reduced if $\mathbf{e}(\theta)$ and $\mathbf{p}$ are orthogonal. From geometric considerations (inserting the θ-dependent polarization $\mathbf{e}(\theta)$ into Eq. (1)) this intensity modulation upon varying θ can be summarized as $I(E,\mathbf{k},\theta) = A + B\sin^2(\theta-\phi_0)$, where the emission angle and the plane of incidence are absorbed into

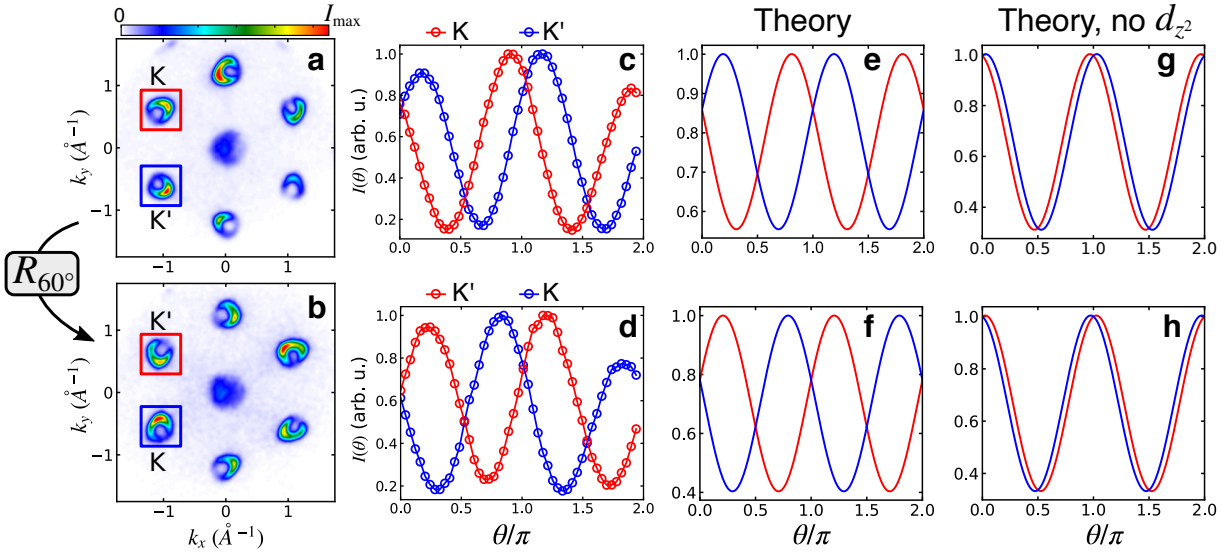

FIG. 2. **Valley-resolved polarization-modulated photoemission: (a)-(b)** Constant energy contours (binding energy $E - E_{\mathrm{VBM}} = -0.25$ eV) for both crystals orientations (averaged over the polarization angle θ). **(c)-(d)**: Valley-resolved polarization-modulated photoemission. **(e)-(f)**: Calculated polarization-angle modulation of the intensity (analogous to **(c)-(d)**). **(g)-(h)**: Analogous to **(e)-(f)**, but excluding the d_{z^2} orbital contribution. The direction of the light incidence is in the y-z plane.

the coefficients A, B. This modulation is generic; however, the position of the maximum – determined by the *phase* ϕ_0 – is extraordinarily sensitive to the initial Bloch state.

The quantum nature of the top valence band of monolayer WSe_2 (or the topmost layer of its 2H-bulk counterpart) can be understood in terms of a few-orbital model comprising the W d_{z^2}, $d_{x^2-y^2}$ and d_{xy} orbitals. We employ the TB model from ref. [31] for all calculations below. Near the valence band maximum (VBM) the Bloch state can be described as $|\psi_{\mathbf{k}}^{\mathrm{K,K'}}\rangle \approx [C_{\pm}(\mathbf{k})|d_{\pm 2}\rangle + C_0(\mathbf{k})|d_{z^2}\rangle] \otimes |\uparrow,\downarrow\rangle$, where $|d_{\pm 2}\rangle = [|d_{x^2-y^2}\rangle \pm i|d_{xy}\rangle]/\sqrt{2}$ are magnetic orbitals. Even though the out-of-plane $|d_{z^2}\rangle$ orbital contribution vanishes at exactly $\mathbf{k} =$ K, K′, the $\mathbf{k}$-dependent interference between these orbitals has profound impact when moving slightly away from $\mathbf{k} =$ K, K′. This orbital texture in momentum-space is captured by the orbital pseudospin $\sigma_\nu^{\mathrm{K,K'}}(\mathbf{k}) = \langle \psi_{\mathbf{k}}^{\mathrm{K,K'}} | \hat{\sigma}_\nu | \psi_{\mathbf{k}}^{\mathrm{K,K'}} \rangle$ ($\hat{\sigma}_\nu$ denote the Pauli matrices). The orbital pseudospin relates to the Berry curvature and topological properties of materials. It manifests itself in the characteristic momentum dependence of the photoemission signal around the high symmetry points [25].

Fig. 1c shows the orbital pseudospin and the associated Bloch wavefunction of WSe_2 localized at the W atom in the vicinity of the K and K′ valley. The mixing of the $|d_{+2}\rangle$ and $|d_{z^2}\rangle$ orbitals leads to a strong $\mathbf{k}$-dependence of the hybridized orbital orientation of the initial state. Experimentally, the photoemission intensity modulation while scanning over all XUV polarization angles θ - $I(E, \mathbf{k}, \theta)$ - serves as a powerful fingerprint of the hybridized orbital orientation, which depends on the relative phase between participating orbitals, and which is reflected in the phase ϕ_0 of the periodic modulation of the photoemission signal with respect to θ.

The experimentally measured photoemission intensity modulation upon varying θ is very pronounced (Fig. 2a–d). The valley-integrated intensity $I_{\mathrm{int}}(E, \theta)$ shows an intrinsic phase shift between K and K′. To confirm that this phase shift is an intrinsic property of the crystals and does not originate from experimental geometry effects, we rotated the crystal by 60°, acting as an effective in-plane time-reversal transformation, *i. e.* K ↔ K′ [32]. Upon effective time-reversal transformation (swapping the valley indexes), the relative phase shift changes sign, indicating that the polarization-modulated photoemission is sensitive to intrinsic valley-resolved properties of the crystal. Apart from the absolute scale, the angular dependence of the photoemission intensity and the phase shifts are well reproduced by our theoretical calculations (Fig. 2e–f). Excluding the d_{z^2} orbitals strongly diminish the intrinsic phase shift between K and K′ valleys (Fig. 2g–h), thus underlining the interplay of d_{z^2} and $d_{\pm 2}$ orbitals in the emergence of the experimentally observed polarization-modulated photoemission signal.

To obtain deeper insights, we have performed a fully energy- and momentum-resolved Fourier transform analysis along the XUV polarization axis in order to extract oscillation amplitude and phase of the signal in specific energy-momentum region of the electronic structure. The Fourier-transformed signal

$$I_m(E, k_x, k_y) = \int_0^{2\pi} \frac{d\theta}{2\pi} e^{im\theta} I(E, k_x, k_y, \theta) \qquad (2)$$

is only nonzero for $m = 0, \pm 2$. While $m = 0$ corresponds to the θ-averaged intensity, $I_2(E, k_x, k_y)$ is a *complex* quantity encoding information about the amplitude/real and phase/imaginary information of the photoemission modulation upon rotating the polarization axis of the XUV. For the

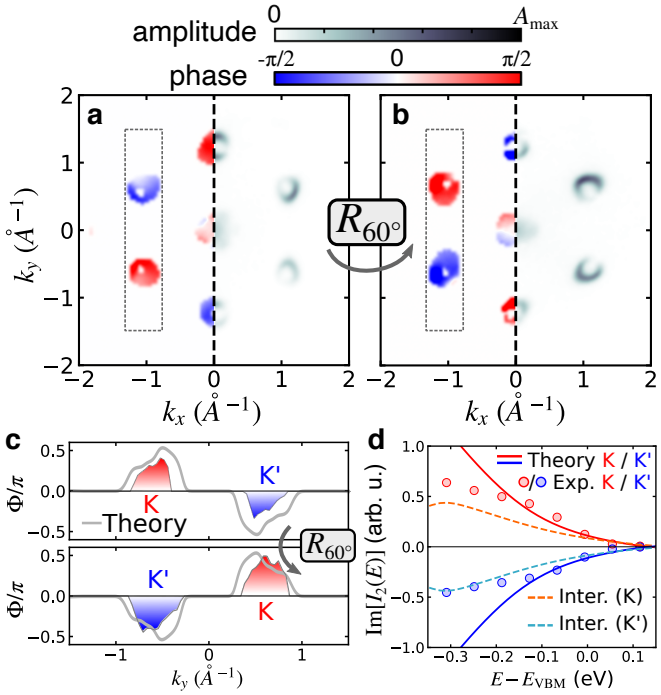

FIG. 3. **Momentum-resolved Fourier analysis of the polarization-modulated ARPES signals: a-b** Fourier amplitude (black and white, right sub-panel, respectively) and phase (red and blue, left sub-panel) of the photoemission modulation, for $E - E_{\mathrm{VBM}}$ = -0.25 eV. **c** Averaged phase (along a vertical cut and integrated over k_x as indicated by the dashed box in **a**,**b**), extracted from both the experimental data in **a-b** and the theory. **d** Valley-integrated imaginary part Im[$I_2(E)$] of the Fourier amplitude (2), comparing experiment and theory at K (red) and K′ (blue), respectively. The dashed lines represent the corresponding interference contribution Im[$I_2^{\mathrm{int}}(E)$].

experimental geometry (Fig. 1a), direct evaluation yields

$$\mathrm{Re}[I_2(E,\mathbf{k})] = \frac{1}{4}\left[|M_s(E,\mathbf{k})|^2 - |M_p(E,\mathbf{k})|^2\right] g(E,\mathbf{k}) \quad (3)$$
$$= \frac{1}{4} I_{\mathrm{LDAD}}(E,\mathbf{k}) \,,$$
$$\mathrm{Im}[I_2(E,\mathbf{k})] = -\frac{1}{2}\mathrm{Re}\left[(M_s(E,\mathbf{k}))^* M_p(E,\mathbf{k})\right] g(E,\mathbf{k}) \,, \quad (4)$$

where $M_s(E,\mathbf{k})$ and $M_p(E,\mathbf{k})$ denote the matrix elements with respect to s- or p- polarized light and where $g(E,\mathbf{k}) = \delta(\varepsilon_{\mathbf{k}\alpha} + \hbar\omega - E)$. While the real part (3) contains information on the linear dichroism of the photoemission intensity with respect to s- or p- polarized light (equivalent to the LDAD), the imaginary part (4) captures *interference* between these channels. We stress that the latter is a new quantity that cannot be obtained by solely measuring the photoemission intensity in s- or p- direction. This interferometric quantity, revealing the relative phase between $M_s(E,\mathbf{k})$ and $M_p(E,\mathbf{k})$, is only available within the context of our novel polarization-modulated ARPES approach.

The energy- and momentum-resolved phase $\Phi(E,\mathbf{k}) = \arg[I_2(E,\mathbf{k})]$ is presented in Fig. 3a–b, for a binding energy of ~ 0.25 eV. Strikingly, we can observe a phase sign-flip for adjacent valleys, as well as a phase sign-flip upon effective time-reversal operation (60° crystal rotation). This is a clear indication that the hybridized orbital orientation (related to orbital pseudospin) – which exhibits a distinct texture at K or K′, respectively – is responsible for the observed sign change. Fig. 3c shows the phase integrated along k_x (going from K to K′, and vice-versa), which is well captured by our TB model calculations.

Inspecting the real (3) and imaginary part (4) of the Fourier signal, we notice that the sign of the phase $\Phi(E,\mathbf{k})$ and Im[$I_2(E,\mathbf{k})$] are qualitatively identical. Comparing the imaginary part to the theoretical results is straightforward (Fig. 3d). The theory allows for decomposing the valley-integrated signal (around the K / K′ valleys in Fig. 3a) into $\mathrm{Im}[I_2(E)] = \mathrm{Im}[I_2^{\mathrm{inc}}(E)] + \mathrm{Im}[I_2^{\mathrm{int}}(E)]$, where the $\mathrm{Im}[I_2^{\mathrm{inc}}(E)] = \mathrm{Im}[I_2^{z^2}(E)] + \mathrm{Im}[I_2^{\pm 2}(E)]$ by incoherently adding signal originating from only the d_{z^2} or $d_{\pm 2}$ orbital, while $\mathrm{Im}[I_2^{\mathrm{int}}(E)]$ denotes the interference contribution. This analysis underpins that the interference of the d_{z^2} and $d_{\pm 2}$ orbitals – which relates to the in-plane pseudospin – is the predominant contribution close to the VBM.

On a more fundamental level, the imaginary part (4) of the polarization-modulated photoemission is the missing piece to measuring the phase of the complex dipole matrix elements directly, if circular dichroism is additionally available. Indeed, let us consider the experimental scheme as in Fig. 1a, but using left-hand circularly polarized (LCP) or right-hand circularly polarized (RCP) light (with respect to the same propagation direction). The circular dichroism in the angular distribution (CDAD) is then defined by $I_{\mathrm{CD}}(E,\mathbf{k}) = I_{\mathrm{LCP}}(E,\mathbf{k}) - I_{\mathrm{RCP}}(E,\mathbf{k})$. Substituting the corresponding polarization vector $\mathbf{e}_{\mathrm{RCP/LCP}}$ into Eq. (1), one obtains

$$I_{\mathrm{CD}}(E,\mathbf{k}) = -2\mathrm{Im}\left[(M_s(E,\mathbf{k}))^* M_p(E,\mathbf{k})\right] g(E,\mathbf{k}) \,. \quad (5)$$

Comparing Eq. (B2) to Eq. (4) we notice a striking similarity: instead of the imaginary part of the complex quantity $Z(E,\mathbf{k}) = (M_s(E,\mathbf{k}))^* M_p(E,\mathbf{k}) = |Z(E,\mathbf{k})| e^{i\gamma(E,\mathbf{k})}$, the imaginary part of the Fourier signal (4) provides access to the real part of $Z(E,\mathbf{k})$. While $|Z(E,\mathbf{k})|$ can be extracted by measuring the photoemission intensity for $s-$ and $p-$ polarized light separately, the relative phase $\gamma(E,\mathbf{k})$ is available by combining the measurent of both the θ-modulation (as in the present experiment) *and* the CDAD. Since the global phase of $M_s(E,\mathbf{k})$ or $M_p(E,\mathbf{k})$ is not relevant (it does not manifest in any observable), obtaining $\gamma(E,\mathbf{k})$ allows extracting complete information on the complex matrix elements $M_{s/p}(E,\mathbf{k})$.

Because the CDAD and the Fourier signal are complementary parts of the same complex quantity, they are fundamentally linked. This intricate relationship can be exploited to the obtain insights into the CDAD without using circularly polarized XUV light. Using Eq. (4), this link can be expressed as

$$\widetilde{I}_{\mathrm{CD}}(E,\mathbf{k}) = \sqrt{I_s(E,\mathbf{k}) I_p(E,\mathbf{k}) - 4\mathrm{Im}[I_2(E,\mathbf{k})]} \,. \quad (6)$$

Note that only the absolute value of the CDAD can be extracted due to a missing absolute phase information to directly link a continuous scan of the linear XUV polarization axis

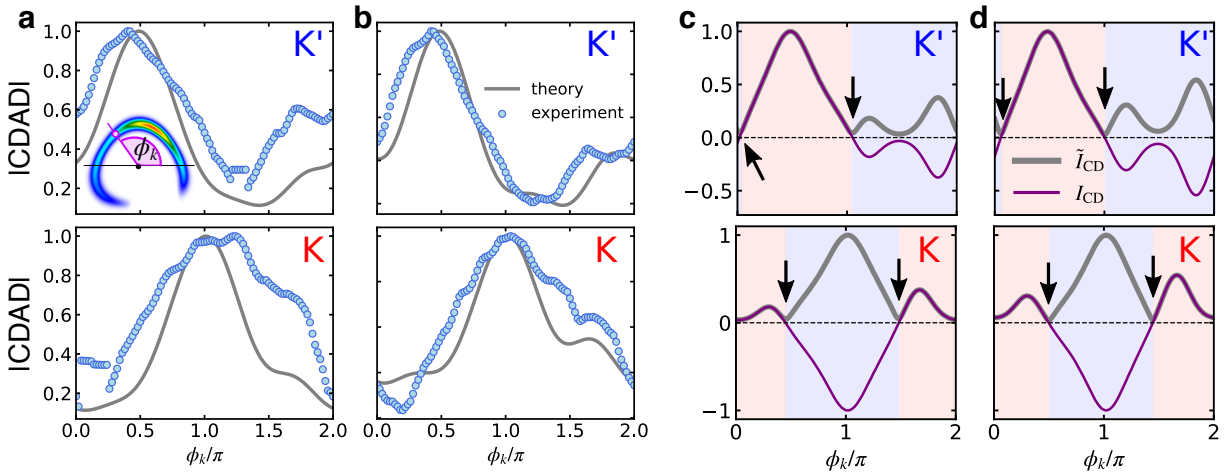

FIG. 4. **Circular dichroism from Fourier signal: a-b** Absolute value of the CDAD extracted from the experimental data and theory via Eq. (6) at fixed binding energy $E - E_{VBM} = -0.18$ eV (a) and $E - E_{VBM} = -0.25$ eV (b), as function the angle ϕ_k tracing the intensity. The inset illustrates how the angle ϕ_k is measured along the contour of maximum intensity. **c-d** Theoretical reconstructed ($\widetilde{I}_{CD}(E,\mathbf{k})$) and calculated CDAD ($I_{CD}(E,\mathbf{k})$) as in **a-b**. The arrows indicate the kink positions that can be used to determine sign changes (indicated by shaded background).

to circularly polarized light (indicated by the tilde in Eq. (6), $|I_{CD}(E,\mathbf{k})| = \widetilde{I}_{CD}(E,\mathbf{k})$). Nevertheless, fine details on the momentum dependence of the circular dichroism can still be extracted as demonstrated in Fig. 4a–b.

To this end we substituted the imaginary part $\mathrm{Im}[I_2(E,\mathbf{k})]$ (obtained by Fourier transforming the experimental data via Eq. (2)) into Eq. (6). Note that the valley-averaged CDAD provides a direct map of the Berry curvature of WSe_2, as demonstrated by previous experiments [16, 17] and theory [18]. However, the CDAD exhibits a fine structure even within a single valley (which depends on the experimental geometry). Thus, for a given binding energy, we show the extracted CDAD as a function of the azimuthal angle ϕ_k, which traces the constant energy contour (see inset in Fig. 4a). By broadening the momentum distribution of the theoretical data to mimic the experimental momentum resolution, we find a striking agreement between experiment and theory for both valleys (Fig. 4a–b). This agreement implies that our novel measurement procedures allow getting information about CDAD, without using circularly polarized pulses.

While the sign of the reconstructed CDAD is, in principle, not available, sharp kinks near zero would indicate a sign change. The momentum resolution of the experiment is not sufficient to identify such sharp features; however, the excellent qualitative agreement between theory and experiment for all considered quantities described above, allows us to extrapolate to a better resolution. This scenario is explored in Fig. 4c–d, where we compare the calculated CDAD to the reconstructed signal (via Eq. (6)). Due to taking the absolute value, kinks (indicated by black arrows) appear in the reconstructed CDAD, which allow pinpointing sign changes. Therefore, up to an absolute sign ambiguity for each valley, the full CDAD can be extracted from our experimental data, where no circularly polarized photons were used.

The complementary information encoded in the imaginary part (4) and the circular dichroism can be exploited even further if the CDAD is measured in the same geometry. The current limitations of our setup do not allow for creating circularly polarized XUV photons. However, complementing the experimental data with the CDAD calculated from our theoretical model – which emulates experimental data – allows us to showcase which new information can be extracted. To this end, we have calculated

$$I_{CD}^{emul}(E,\mathbf{k}) = \frac{I_{CD}^{TB}(E,\mathbf{k})}{I_{av}^{TB}(E,\mathbf{k})} I_{av}^{exp}(E,\mathbf{k}) \,, \tag{7}$$

where $I_{av}(E,\mathbf{k}) = (I_s(E,\mathbf{k}) + I_p(E,\mathbf{k}))/2$ is the unpolarized intensity. The superscript TB (exp) stands for theoretical (experimental) spectra. The TB model includes two orbitals only (d_{z^2} and $d_{\pm 2}$), such that the Bloch state $|\psi_{\mathbf{k}\alpha}^{K,K'}\rangle$ is fully characterized by the three components of pseudospin $\sigma_\nu^{K,K'}(\mathbf{k})$ ($\nu = 1,2,3$). It is convenient to express the photoemission intensity (1) in terms of $\sigma_\nu^{K,K'}(\mathbf{k})$ and the atomic dipole matrix elements $M_{z^2,\pm 2}(E,\mathbf{k}) = \langle \mathbf{k}, E|\mathbf{e}\cdot\hat{\mathbf{r}}|d_{z^2,\pm 2}\rangle$. Approximating the orbitals as product of a radial wavefunction and a spherical harmonic $Y_{0,\pm 2}^2$ allows to characterize $M_{z^2,\pm 2}(E,\mathbf{k})$ by a few parameters, which can be fixed by comparing to experimental spectra with $s-$ and $p-$ polarized light, respectively. Since we also have three independent quantities $\mathbf{X}(E,\mathbf{k}) = (I_{CD}(E,\mathbf{k}), \mathrm{Re}[I_2(E,\mathbf{k})], \mathrm{Im}[I_2(E,\mathbf{k})])$ at our disposal, can we use this information to reconstruct the three-dimensional orbital pseudospin? The answer is affirmative, as demonstrated in Fig. 5.

Based on the atomic matrix elements $M_{z^2,\pm 2}(E,\mathbf{k})$, we can express the CDAD and the Fourier signal as linear functions of $\sigma_\nu^{K,K'}(\mathbf{k})$, which yields a 3×3 system of equations of the form $\mathbf{X}(E,\mathbf{k}) = \mathbf{A}(E,\mathbf{k})\boldsymbol{\sigma}^{K,K'}(\mathbf{k}) + \mathbf{B}(E,\mathbf{k})$, as detailed in the SM. We have solved these equations – using the calculated matrix

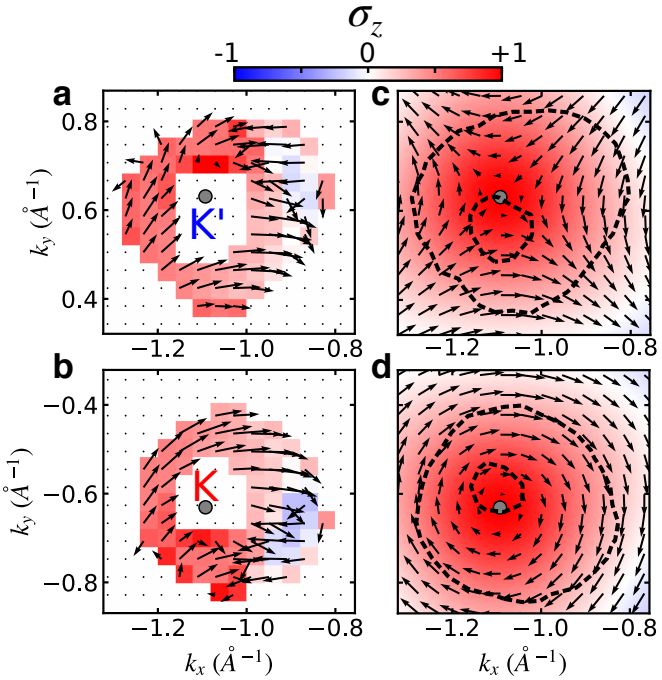

FIG. 5. **Reconstruction of orbital pseudospin: (a)-(b)** Pseudospin texture reconstructed from experimental (with emulated CDAD) data. The in-plane pseudospin is represented by the arrows, while the z-component is indicated by the color map. We present results for $E - E_{\mathrm{VBM}} = -0.25$ eV, where the reconstruction procedure is most stable.**(c)-(d)** Orbital pseudospin from the TB model. The black dashed lines indicate the region in which the intensity $I_{\mathrm{av}}(E, \mathbf{k}) > 0.1 I_{\mathrm{max}}$ (I_{max} is the maximum intensity).

elements, the experimental Fourier signal and the emulated CDAD – by a least-square minimization while constraining the pseudospin to $\sum_\nu (\sigma_\nu^{\mathrm{K,K'}}(\mathbf{k}))^2 = 1$. This is possible for all momenta $\mathbf{k}$ where the signal at fixed binding energy is large enough (we chose a threshold of 0.1 of the maximum value). The reconstructed pseudospin for the $E - E_{\mathrm{VBM}} = -0.25$ eV is presented in Fig. 5a-b for K and K′, respectively. Scanning through the binding energies allows, in principle, to systematically reconstruct the pseudospin texture in the relevant region in momentum space, albeit the pseudospin picture (i. e. where only two orbitals are relevant) breaks down further away from K/K′. Comparing the reconstructed texture of $\sigma_\nu^{\mathrm{K,K'}}(\mathbf{k})$ to the calculated one (Fig. 5c–d), good qualitative agreement is observed. For $\sigma_\nu^{\mathrm{K'}}(\mathbf{k})$ the vortex structure of the pseudospin pattern (Fig. 5c) is retained, while the in-plane circular winding at K is obtained (comparing Fig. 5b to d). Also, the z-component (which captures that relative weight of the d_{z^2} orbital) is in good qualitative agreement with the theory, including the decreasing value further away from the VBM. Deviations are mostly attributed to two factors: (i) the momentum and energy resolution, and (ii) limited predictive power of the photoemission model. Systematic improvements of photoemission dipole matrix elements – and thus the retrieval of $\sigma_\nu^{\mathrm{K,K'}}(\mathbf{k})$ – beyond the presented model can be achieved by more accurate calculation of the final states and by taking into account non-spherical deformations of the Wannier orbitals.

We stress that in principle, besides the atomic matrix elements, no further input from theory is required. In particular, the band structure does not enter the reconstruction procedure. Hence, a practical route for applying the procedure to other systems is to fit the atomic matrix elements to specific features in equilibrium (for instance, our atomistic model for WSe_2 reproduces the dark corridor). The thus obtained matrix elements are the only required theoretical input for tracing the impact of light-dressing, coherent excitation, or strain onto the pseudospin texture. Since the modeling of the atomic matrix elements is generic, the presented reconstruction procedure can be applied to many systems where a few relevant orbitals are involved.

DISCUSSION/CONCLUSION

Our novel measurement methodology in photoemission spectroscopy allows the reconstruction of the orbital pseudospin and thus – exploiting the one-to-one correspondence – of the complex-valued Bloch wavefunction in solids. Our scheme also allows extracting the absolute value of XUV-CDAD without using circularly polarized XUV pulses. This is a major advance since the table-top generation of circularly polarized XUV is challenging and its combination with ARPES endstation has not been reported yet. The extension of our approach to time-resolved CDAD experiments without the need of circular XUV photons, and time-resolved Bloch wavefunction reconstruction is conceptually straightforward, which will allow tracking ultrafast light-induced topological phase transition characterized by creation or annihilation of local Berry curvature [33–37]. Moreover, because of the simplicity of the theoretical model, the joint experimental and theoretical machinery that we introduced can be applied to solve open questions about the detailed (topological) nature of electronic structures of some solids, which are still under debate, *e.g.* 1T'-WTe_2 [38], nonsymmorphic crystals without gaps [39] or light-induced topological states in graphene and Weyl semimetal [34]. Our work can be seen as the first condensed matter "complete" photoionization experiments, in which one obtains the full complex photoemission dipole matrix element, which is already established as the grail of a photoionization experiment in atomic and molecular physics [2, 40, 41].

METHODS

A. Multidimensional photoemission spectroscopy

The multidimensional photoemission spectroscopy experiments were performed at the Fritz Haber Institute of the Max Planck Society. We used a home-built optical parametric chirped-pulse amplifier (OPCPA) delivering 30 μJ/pulses (800 nm, 30 fs) at 500 kHz repetition rate [42]. The second harmonic of the OPCPA output (400 nm) is used to drive high-order harmonic generation (HHG) by tightly focusing (15 μm

FWHM) laser pulses onto a thin and dense Argon gas jet, using a perforated focusing mirror (f=100 mm) with a 1.5 mm hole diameter. The extremely nonlinear interaction between the laser pulses and the Argon atoms leads to the generation of a comb of odd harmonics of the driving laser, extending up to the 11th order. Because the XUV harmonics are generated using an annular driving beam, the copropagating fundamental (400 nm) can be separated from the XUV harmonic beam using a spatial filter (iris) in the far-field. Using this geometry, one can avoid the typically used reflection onto a silicon wafer at Brewster's angle to filter out the energy of the fundamental driving laser, which only works for p-polarized light. Thus, the annular beam HHG scheme allows us to continuously rotate the polarization of the XUV, by simply rotating the polarization of the 400 nm in front of the HHG chamber using a $\lambda/2$-waveplate. Next, a single harmonic (7th order, 21.7 eV) is isolated by reflection off a focusing multilayer XUV mirror and transmission through a 400 nm thick Sn metallic filter. A photon flux of up to $2\text{x}10^{11}$ photons/s at the sample position is obtained (110 meV FWHM)[29]. The bulk WSe_2 samples are handled by a 6-axis manipulator (SPECS GmbH) and cleaved at a base pressure of $5\text{x}10^{-11}$ mbar. The data are acquired using a time-of-flight momentum microscope (METIS1000, SPECS GmbH), allowing to detect each photoelectron as a single event and as a function of XUV linear polarization angle (θ) [30, 43].

B. Tight-binding calculations of photoemission

All theoretical results were obtained from the tight-binding (TB) model from ref. [31], which reproduces the band structure and orbital character in the vicinity of the valleys very well. We included the d_{z^2}, d_{xy} and $d_{x^2-y^2}$ orbitals at the W sites. For convenience we transformed to the magnetic basis $d_{\pm 2} \equiv (d_{x^2-y^2} \pm i d_{xy})/\sqrt{2}$. The atomic photoemission matrix elements are obtained within the plane-wave (PW) approximation to the final states while representing the dipole operator by the position operator $\mathbf{r}$ with respect to the W sites. This dipole gauge has been shown to be qualitatively accurate for various systems [18, 44]. Within this approximation, the matrix elements are obtained from

$$M_m(E,\mathbf{k}) = \int d\mathbf{r}\, e^{-i\mathbf{k}\cdot\mathbf{r}} e^{-ik_\perp z} \mathbf{e}\cdot\mathbf{r}\, w_m(\mathbf{r})\,, \qquad (8)$$

where $m = z^2, \pm 2$ and where $w_m(\mathbf{r})$ denotes the corresponding atomic orbital. The out-of-plane momentum $k_\perp$ is determined by energy conservation. The atomic orbitals are approximated by $w_m(\mathbf{r}) \approx f(r) Y_{\ell=2,m}(\hat{r})$. The radial dependence is estimated by comparing to density-functional theory calculations (as in ref. [25]). The matrix elements with respect to the Bloch states $|\psi_{\mathbf{k}\alpha}\rangle$ (which enter the Fermi Golden rule (1)) are then calculated by $M(E,\mathbf{k}) = \sum_m C_m(\mathbf{k}) M_m(E,\mathbf{k})$, where the coefficients $C_m(\mathbf{k})$ are obtained from the TB Hamiltonian.

This TB+PW model has been benchmarked for this system in ref. [25] against experimental results and first-principle calculations, which corroborated its predictive power. Furthermore, we showed that considering a monolayer WSe_2 and omitting spin-orbit coupling is sufficient to reproduce the photoemission signal of the top valence band.

[1] D. Shafir, Y. Mairesse, D. M. Villeneuve, P. B. Corkum, and N. Dudovich, "Atomic wavefunctions probed through strong-field light–matter interaction," Nature Phys. **5**, 412–416 (2009).

[2] D. M. Villeneuve, Paul Hockett, M. J. J. Vrakking, and Hiromichi Niikura, "Coherent imaging of an attosecond electron wave packet," Science **356**, 1150–1153 (2017).

[3] J. Itatani, J. Levesque, D. Zeidler, Hiromichi Niikura, H. Pépin, J. C. Kieffer, P. B. Corkum, and D. M. Villeneuve, "Tomographic imaging of molecular orbitals," Nature **432**, 867–871 (2004).

[4] S. Haessler, J. Caillat, W. Boutu, C. Giovanetti-Teixeira, T. Ruchon, T. Auguste, Z. Diveki, P. Breger, A. Maquet, B. Carré, R. Taïeb, and P. Salières, "Attosecond imaging of molecular electronic wavepackets," Nature Phys. **6**, 200–206 (2010).

[5] Peter Puschnig, Stephen Berkebile, Alexander J. Fleming, Georg Koller, Konstantin Emtsev, Thomas Seyller, John D. Riley, Claudia Ambrosch-Draxl, Falko P. Netzer, and Michael G. Ramsey, "Reconstruction of molecular orbital densities from photoemission data," Science **326**, 702–706 (2009).

[6] M. Wießner, D. Hauschild, C. Sauer, V. Feyer, A. Schöll, and F. Reinert, "Complete determination of molecular orbitals by measurement of phase symmetry and electron density," Nature Communications **5**, 4156 (2014).

[7] Michael K. L. Man, Julien Madéo, Chakradhar Sahoo, Kaichen Xie, Marshall Campbell, Vivek Pareek, Arka Karmakar, E Laine Wong, Abdullah Al-Mahboob, Nicholas S. Chan, David R. Bacon, Xing Zhu, Mohamed Abdelrasoul, Xiaoquin Li, Tony F. Heinz, Felipe H. da Jornada, Ting Cao, and Keshav M. Dani, "Experimental measurement of the intrinsic excitonic wavefunction," (2020), arXiv:2011.13104 [cond-mat.mes-hall].

[8] Shuo Dong, Michele Puppin, Tommaso Pincelli, Samuel Beaulieu, Dominik Christiansen, Hannes Hubener, Christopher W. Nicholson, R. Patrick Xian, Maciej Dendzik, Yunpei Deng, Yoav William Windsor, Malte Selig, Ermin Malic, Angel Rubio, Andreas Knorr, Martin Wolf, Laurenz Rettig, and Ralph Ernstorfer, "Measurement of an excitonic wave function," (2020), arXiv:2012.15328 [cond-mat.mtrl-sci].

[9] C. L. Kane and E. J. Mele, "Z_2 topological order and the quantum spin hall effect," Phys. Rev. Lett. **95**, 146802 (2005).

[10] Michael Victor Berry, "Quantal phase factors accompanying adiabatic changes," Proceedings of the Royal Society of London. A. Mathematical and Physical Sciences **392**, 45–57 (1984).

[11] Andrea Damascelli, "Probing the electronic structure of complex systems by ARPES," Phys. Scr. **T109**, 61 (2004).

[12] Y. Liu, G. Bian, T. Miller, and T.-C. Chiang, "Visualizing electronic chirality and berry phases in graphene systems using photoemission with circularly polarized light," Phys. Rev. Lett. **107**,

166803 (2011).
[13] Y. H. Wang, D. Hsieh, D. Pilon, L. Fu, D. R. Gardner, Y. S. Lee, and N. Gedik, "Observation of a warped helical spin texture in Bi_2Se_3 from circular dichroism angle-resolved photoemission spectroscopy," Phys. Rev. Lett. **107**, 207602 (2011).
[14] Jin-Hong Park, Choong H. Kim, Jun-Won Rhim, and Jung Hoon Han, "Orbital rashba effect and its detection by circular dichroism angle-resolved photoemission spectroscopy," Phys. Rev. B **85**, 195401 (2012).
[15] E. Razzoli, T. Jaouen, M.-L. Mottas, B. Hildebrand, G. Monney, A. Pisoni, S. Muff, M. Fanciulli, N. C. Plumb, V. A. Rogalev, V. N. Strocov, J. Mesot, M. Shi, J. H. Dil, H. Beck, and P. Aebi, "Selective Probing of Hidden Spin-Polarized States in Inversion-Symmetric Bulk MoS_2," Phys. Rev. Lett. **118**, 086402 (2017).
[16] Soohyun Cho, Jin-Hong Park, Jisook Hong, Jongkeun Jung, Beom Seo Kim, Garam Han, Wonshik Kyung, Yeongkwan Kim, S.-K. Mo, J. D. Denlinger, Ji Hoon Shim, Jung Hoon Han, Changyoung Kim, and Seung Ryong Park, "Experimental Observation of Hidden Berry Curvature in Inversion-Symmetric Bulk 2H-WSe_2," Phys. Rev. Lett. **121**, 186401 (2018).
[17] Soohyun Cho, Jin-Hong Park, Soonsang Huh, Jisook Hong, Wonshik Kyung, Byeong-Gyu Park, J. D. Denlinger, Ji Hoon Shim, Changyoung Kim, and Seung Ryong Park, "Studying local Berry curvature in 2H-WSe_2 by circular dichroism photoemission utilizing crystal mirror plane," Scientific Reports **11**, 1684 (2021).
[18] Michael Schüler, Umberto De Giovannini, Hannes Hübener, Angel Rubio, Michael A. Sentef, and Philipp Werner, "Local Berry curvature signatures in dichroic angle-resolved photoelectron spectroscopy from two-dimensional materials," Science Advances **6**, eaay2730 (2020).
[19] Gerd Schönhense, "Circular dichroism and spin polarization in photoemission from adsorbates and non-magnetic solids," Phys. Scr. **T31**, 255–275 (1990).
[20] N. A Cherepkov and G Schönhense, "Linear dichroism in photoemission from oriented molecules," Europhys. Lett. **24**, 79–85 (1993).
[21] A. Sterzi, G. Manzoni, A. Crepaldi, F. Cilento, M. Zacchigna, M. Leclerc, Ph. Bugnon, A. Magrez, H. Berger, L. Petaccia, and F. Parmigiani, "Probing band parity inversion in the topological insulator $GeBi_2Te_4$ by linear dichroism in arpes," Journal of Electron Spectroscopy and Related Phenomena **225**, 23 – 27 (2018).
[22] Klara Volckaert, Habib Rostami, Deepnarayan Biswas, Igor Marković, Federico Andreatta, Charlotte E. Sanders, Paulina Majchrzak, Cephise Cacho, Richard T. Chapman, Adam Wyatt, Emma Springate, Daniel Lizzit, Luca Bignardi, Silvano Lizzit, Sanjoy K. Mahatha, Marco Bianchi, Nicola Lanata, Phil D. C. King, Jill A. Miwa, Alexander V. Balatsky, Philip Hofmann, and Søren Ulstrup, "Momentum-resolved linear dichroism in bilayer MoS_2," Phys. Rev. B **100**, 241406 (2019).
[23] Xiuwen Zhang, Qihang Liu, Jun-Wei Luo, Arthur J. Freeman, and Alex Zunger, "Hidden spin polarization in inversion-symmetric bulk crystals," Nature Phys. **10**, 387–393 (2014).
[24] J. M. Riley, F. Mazzola, M. Dendzik, M. Michiardi, T. Takayama, L. Bawden, C. Granerød, M. Leandersson, T. Balasubramanian, M. Hoesch, T. K. Kim, H. Takagi, W. Meevasana, Ph Hofmann, M. S. Bahramy, J. W. Wells, and P. D. C. King, "Direct observation of spin-polarized bulk bands in an inversion-symmetric semiconductor," Nature Phys. **10**, 835–839 (2014).
[25] S. Beaulieu, J. Schusser, S. Dong, M. Schüler, T. Pincelli, M. Dendzik, J. Maklar, A. Neef, H. Ebert, K. Hricovini, M. Wolf, J. Braun, L. Rettig, J. Minár, and R. Ernstorfer, "Revealing Hidden Orbital Pseudospin Texture with Time-Reversal Dichroism in Photoelectron Angular Distributions," Phys. Rev. Lett. **125**, 216404 (2020).
[26] R. Bertoni, C. W. Nicholson, L. Waldecker, H. Hübener, C. Monney, U. De Giovannini, M. Puppin, M. Hoesch, E. Springate, R. T. Chapman, C. Cacho, M. Wolf, A. Rubio, and R. Ernstorfer, "Generation and evolution of spin-, valley-, and layer-polarized excited carriers in inversion-symmetric WSe_2," Phys. Rev. Lett. **117**, 277201 (2016).
[27] Dongwook Go, Daegeun Jo, Changyoung Kim, and Hyun-Woo Lee, "Intrinsic spin and orbital hall effects from orbital texture," Phys. Rev. Lett. **121**, 086602 (2018).
[28] Luis M. Canonico, Tarik P. Cysne, Alejandro Molina-Sanchez, R. B. Muniz, and Tatiana G. Rappoport, "Orbital hall insulating phase in transition metal dichalcogenide monolayers," Phys. Rev. B **101**, 161409 (2020).
[29] M. Puppin, Y. Deng, C. W. Nicholson, J. Feldl, N. B. M. Schröter, H. Vita, P. S. Kirchmann, C. Monney, L. Rettig, M. Wolf, and R. Ernstorfer, "Time- and angle-resolved photoemission spectroscopy of solids in the extreme ultraviolet at 500 khz repetition rate," Review of Scientific Instruments **90**, 023104 (2019).
[30] J. Maklar, S. Dong, S. Beaulieu, T. Pincelli, M. Dendzik, Y. W. Windsor, R. P. Xian, M. Wolf, R. Ernstorfer, and L. Rettig, "A quantitative comparison of time-of-flight momentum microscopes and hemispherical analyzers for time- and angle-resolved photoemission spectroscopy experiments," Review of Scientific Instruments **91**, 123112 (2020).
[31] Gui-Bin Liu, Wen-Yu Shan, Yugui Yao, Wang Yao, and Di Xiao, "Three-band tight-binding model for monolayers of group-VIB transition metal dichalcogenides," Phys. Rev. B **88**, 085433 (2013).
[32] Shiang Fang, Rodrick Kuate Defo, Sharmila N. Shirodkar, Simon Lieu, Georgios A. Tritsaris, and Efthimios Kaxiras, "Ab initio tight-binding Hamiltonian for transition metal dichalcogenides," Phys. Rev. B **92**, 205108 (2015).
[33] Liang Luo, Di Cheng, Boqun Song, Lin-Lin Wang, Chirag Vaswani, P. M. Lozano, G. Gu, Chuankun Huang, Richard H. J. Kim, Zhaoyu Liu, Joong-Mok Park, Yongxin Yao, Kaiming Ho, Ilias E. Perakis, Qiang Li, and Jigang Wang, "A light-induced phononic symmetry switch and giant dissipationless topological photocurrent in $ZrTe_5$," Nat. Mater. **20**, 329–334 (2021).
[34] Edbert J. Sie, Clara M. Nyby, C. D. Pemmaraju, Su Ji Park, Xiaozhe Shen, Jie Yang, Matthias C. Hoffmann, B. K. Ofori-Okai, Renkai Li, Alexander H. Reid, Stephen Weathersby, Ehren Mannebach, Nathan Finney, Daniel Rhodes, Daniel Chenet, Abhinandan Antony, Luis Balicas, James Hone, Thomas P. Devereaux, Tony F. Heinz, Xijie Wang, and Aaron M. Lindenberg, "An ultrafast symmetry switch in a Weyl semimetal," Nature **565**, 61–66 (2019).
[35] M. A. Sentef, M. Claassen, A. F. Kemper, B. Moritz, T. Oka, J. K. Freericks, and T. P. Devereaux, "Theory of floquet band formation and local pseudospin textures in pump-probe photoemission of graphene," Nature Communications **6**, 7047 (2015).
[36] Hannes Hübener, Michael A. Sentef, Umberto De Giovannini, Alexander F. Kemper, and Angel Rubio, "Creating stable floquet–weyl semimetals by laser-driving of 3d dirac materials," Nature Communications **8**, 13940 (2017).
[37] Michael Schüler, Umberto De Giovannini, Hannes Hübener, Angel Rubio, Michael A. Sentef, Thomas P. Devereaux, and Philipp Werner, "How circular dichroism in time- and angle-resolved photoemission can be used to spectroscopically detect transient topological states in graphene," Phys. Rev. X **10**,

041013 (2020).
[38] Shujie Tang, Chaofan Zhang, Dillon Wong, Zahra Pedramrazi, Hsin-Zon Tsai, Chunjing Jia, Brian Moritz, Martin Claassen, Hyejin Ryu, Salman Kahn, Juan Jiang, Hao Yan, Makoto Hashimoto, Donghui Lu, Robert G. Moore, Chan-Cuk Hwang, Choongyu Hwang, Zahid Hussain, Yulin Chen, Miguel M. Ugeda, Zhi Liu, Xiaoming Xie, Thomas P. Devereaux, Michael F. Crommie, Sung-Kwan Mo, and Zhi-Xun Shen, "Quantum spin Hall state in monolayer 1T'-WTe_2," Nature Phys. **13**, 683–687 (2017).
[39] Lukas Muechler, A. Alexandradinata, Titus Neupert, and Roberto Car, "Topological Nonsymmorphic Metals from Band Inversion," Phys. Rev. X **6**, 041069 (2016).
[40] N.A. Cherepkov, "Complete experiments in photoionization of atoms and molecules," Journal of Electron Spectroscopy and Related Phenomena **144-147**, 1197–1201 (2005).
[41] P. Hockett, M. Wollenhaupt, C. Lux, and T. Baumert, "Complete photoionization experiments via ultrafast coherent control with polarization multiplexing," Phys. Rev. Lett. **112**, 223001 (2014).
[42] Michele Puppin, Yunpei Deng, Oliver Prochnow, Jan Ahrens, Thomas Binhammer, Uwe Morgner, Marcel Krenz, Martin Wolf, and Ralph Ernstorfer, "500 khz opcpa delivering tunable sub-20 fs pulses with 15 w average power based on an all-ytterbium laser," Opt. Express **23**, 1491–1497 (2015).
[43] K. Medjanik, O. Fedchenko, S. Chernov, D. Kutnyakhov, M. Ellguth, A. Oelsner, B. Schönhense, T. R. F. Peixoto, P. Lutz, C.-H. Min, F. Reinert, S. Däster, Y. Acremann, J. Viefhaus, W. Wurth, H. J. Elmers, and G. Schönhense, "Direct 3d mapping of the fermi surface and fermi velocity," Nat. Mater. **16**, 615–621 (2017).
[44] Ryan P. Day, Berend Zwartsenberg, Ilya S. Elfimov, and Andrea Damascelli, "Computational framework chinook for angle-resolved photoemission spectroscopy," npj Quantum Materials **4**, 1–10 (2019).

ACKNOWLEDGMENTS

This work was funded by the Max Planck Society, the European Research Council (ERC) under the European Union's Horizon 2020 research and innovation program (Grant No. ERC-2015-CoG-682843 and H2020-FETOPEN-2018-2019-2020-01 (OPTOLogic - grant agreement No. 899794)), the German Research Foundation (DFG) within the Emmy Noether program (Grant No. RE 3977/1), the Collaborative Research Center/Transregio 227 "Ultrafast Spin Dynamics" (project B07 and A09) and the Priority Program SPP 2244 (project No. 443366970), and the U.S. Department of Energy (DOE), Office of Basic Energy Sciences, Division of Materials Sciences and Engineering, under contract DE-AC02-76SF00515. T. P. acknowledges financial support from the Alexander von Humboldt Fellowship program of the Alexander von Humboldt Stiftung. M.S. thanks the Alexander von Humboldt Foundation for its support with a Feodor Lynen scholarship. S.B. acknowledges financial support from the NSERC-Banting Postdoctoral Fellowships Program.

AUTHOR CONTRIBUTIONS

S.B., T.P. and S.D. performed the multidimensional photoemission spectroscopy experiments. S.B. analyzed and interpreted the experimental data. R.E., L.R. and M.W. were responsible for developing the infrastructures allowing these measurements as well as for the overall project direction. M.S. performed the theoretical calculations, their analysis and interpretation, with the guidance of T.P.D.. M.S. and S.B. wrote the first draft of the manuscript. All authors contributed to the discussions and the final version of the manuscript.

COMPETING INTERESTS

The authors declare that they have no competing financial interests.

SUPPLEMENTARY INFORMATION

Appendix A: Details on the theoretical modeling

The electronic structure is described by the three-band tight-binding (TB) model from ref. [31] comprising the d_{z^2}, $d_{x^2-y^2}$ and the d_{xy} orbitals at the tungsten sites. For convenience we perform the rotation to the magnetic basis, using the d_{z^2} (magnetic quantum number $m = 0$) and the $d_{\pm 2}$ (magnetic quantum number $m = \pm 2$) as basis functions. The Bloch wavefunction of the top valence band $\alpha = v$ (omitting the spin state) is then approximated as

$$\begin{aligned}\psi_{\mathbf{k}\alpha}(\mathbf{r}) &= \frac{1}{\sqrt{N}} \sum_{m=0,\pm 2} C_m(\mathbf{k}) \sum_{\mathbf{R}} e^{i\mathbf{k}\cdot\mathbf{R}} w_m(\mathbf{r}-\mathbf{R}) \qquad \text{(A1)}\\ &\equiv \sum_{m=0,\pm 2} C_m(\mathbf{k}) \phi_{\mathbf{k}m}(\mathbf{r}) \,,\end{aligned}$$

where the coefficients $C_m(\mathbf{k})$ are obtained from the corresponding eigenvector of the TB Hamiltonian $H(\mathbf{k})$. The Wannier functions $w_m(\mathbf{r})$ are approximated by the simple atomic orbitals $w_m(\mathbf{r}) = R_m(r)Y_{2,m}(\hat{\mathbf{r}})$ ($Y_{l,m}(\hat{\mathbf{r}})$ denotes the spherical harmonics). We use the same radial dependence as in ref. [25], where the TB model and parameterization of the orbitals has been benchmarked against first-principle calculations. To express photoemission matrix elements with respect to the Bloch state (A1) it is convenient to introduce the atomic matrix elements

$$M_m^{s,p}(E,\mathbf{k}) = \int d\mathbf{r}\, e^{-i\mathbf{k}\cdot\mathbf{r}} e^{-ip_\perp z} \mathbf{e}_{s,p}\cdot\mathbf{r}\, w_m(\mathbf{r}) \,, \qquad \text{(A2)}$$

which we evaluate by expanding the plane-wave final state in terms of spherical harmonics. The out-of-plane momentum $p_\perp$ is determined by the kinetic energy of the final state $E = \mathbf{k}^2/2 + p_\perp^2/2$. The matrix elements (A2) are defined for s (p) polarized light, parameterized by the unit vector $\mathbf{e}_s$ ($\mathbf{e}_p$). For the experimental geometry (see. Fig. 1a in the main text), these vectors are defined by $\mathbf{e}_s = \mathbf{e}_x$ and $\mathbf{e}_p = -\cos\alpha\mathbf{e}_y +$

$\sin\alpha\mathbf{e}_z$, where $\mathbf{e}_r$ ($r = x, y, z$) stands for the corresponding unit vector, and where $\alpha = 65°$ is the angle of incidence.

From the atomic matrix elements (A2) we can calculate the matrix elements with respect to the initial Bloch state by

$$M^{s,p}(E,\mathbf{k}) = \sum_{m=0,\pm2} C_m(\mathbf{k}) M_m^{s,p}(E,\mathbf{k}) \,. \tag{A3}$$

All quantities discussed in the main text – circular dichroism and the Fourier signal – can be expressed in terms of the matrix elements (A3).

Appendix B: Reconstruction of the orbital pseudospin

The orbital pseudospin completely determines the photoemission signal, including the circular dichorism, the linear dichroism, and the Fourier signal. Close to the valence band maximum ($\mathbf{k} \approx$ K or $\mathbf{k} \approx$ K′) the Bloch state (A1) is well approximated by. $|\psi_{\mathbf{k}\alpha}^{\mathrm{K,K'}}\rangle = C_0(\mathbf{k})|\phi_{\mathbf{k}0}\rangle + C_{\pm2}(\mathbf{k})|\phi_{\mathbf{k}\pm2}\rangle$. The corresponding orbital pseudospin is defined by $\sigma_\nu^{\mathrm{K,K'}}(\mathbf{k}) = \langle\psi_{\mathbf{k}\alpha}^{\mathrm{K,K'}}|\hat{\sigma}_\nu|\psi_{\mathbf{k}\alpha}^{\mathrm{K,K'}}\rangle$. The one-to-one correspondence of the complex coefficients $C_m(\mathbf{k})$ and the orbital pseudospin is given by

$$\sigma_x^{\mathrm{K,K'}}(\mathbf{k}) = 2\mathrm{Re}[C_{\pm2}^*(\mathbf{k})C_0(\mathbf{k})] \,, \tag{B1a}$$

$$\sigma_y^{\mathrm{K,K'}}(\mathbf{k}) = 2\mathrm{Im}[C_{\pm2}^*(\mathbf{k})C_0(\mathbf{k})] \,, \tag{B1b}$$

$$\sigma_z^{\mathrm{K,K'}}(\mathbf{k}) = |C_{\pm2}(\mathbf{k})|^2 - |C_0(\mathbf{k})|^2 \,. \tag{B1c}$$

Now we relate the photoemission signal to the pseudospin via Eq. (B1). We start from the circular dichroism, which is given by (cf. Eq. (5) in the main text) as

$$I_{\mathrm{CD}}(E,\mathbf{k}) = -2\mathrm{Im}[(M^s(E,\mathbf{k}))^* M^p(E,\mathbf{k})] g(E,\mathbf{k}) \,. \tag{B2}$$

Here $g(E,\mathbf{k})$ contains the energy conservation. In theory, this factor reduces to a Dirac delta function, but for practical calculations we replace it by a Gaussian function when calculating the CDAD (B2) (or any other intensity).

Inserting Eq. (A3) and expressing the complex products of the coefficients in terms of the pseudospin via Eqs. (B1), one obtains the linear expression

$$I_{\mathrm{CD}}(E,\mathbf{k}) = \left(\sum_{\nu=1,2,3} A_{\mathrm{CD},\nu}^{\mathrm{K,K'}}(E,\mathbf{k}) \sigma_\nu^{\mathrm{K,K'}}(\mathbf{k}) + B_{\mathrm{CD}}^{\mathrm{K,K'}}(E,\mathbf{k}) \right) \times g(E,\mathbf{k}) \,. \tag{B3}$$

The coefficients in front of the pseudospin are given by

$$A_{\mathrm{CD},x}^{\mathrm{K,K'}}(E,\mathbf{k}) = -\left(\mathrm{Im}[(M_0^s(E,\mathbf{k}))^* M_{\pm2}^p(E,\mathbf{k})] + \mathrm{Im}[(M_{\pm2}^s(E,\mathbf{k}))^* M_0^p(E,\mathbf{k})] \right) \,, \tag{B4a}$$

$$A_{\mathrm{CD},y}^{\mathrm{K,K'}}(E,\mathbf{k}) = \mathrm{Re}[(M_0^s(E,\mathbf{k}))^* M_{\pm2}^p(E,\mathbf{k})] - \mathrm{Re}[(M_{\pm2}^s(E,\mathbf{k}))^* M_0^p(E,\mathbf{k})] \,, \tag{B4b}$$

$$A_{\mathrm{CD},z}^{\mathrm{K,K'}}(E,\mathbf{k}) = \mathrm{Im}[(M_0^s(E,\mathbf{k}))^* M_{\pm2}^p(E,\mathbf{k})] - \mathrm{Im}[(M_{\pm2}^s(E,\mathbf{k}))^* M_0^p(E,\mathbf{k})] \,, \tag{B4c}$$

while

$$B_{\mathrm{CD}}^{\mathrm{K,K'}}(E,\mathbf{k}) = -\left(\mathrm{Im}[(M_0^s(E,\mathbf{k}))^* M_0^p(E,\mathbf{k})] + \mathrm{Im}[(M_{\pm2}^s(E,\mathbf{k}))^* M_{\pm2}^p(E,\mathbf{k})] \right) \,. \tag{B5}$$

The expression (B3) is generic – any intensity can be expressed in a similar linear form with respect to the pseudospin. Following the analogous route for the real part of the Fourier signal, we find

$$\mathrm{Re}[I_2(E,\mathbf{k})] = \left(\sum_{\nu=1,2,3} A_{\mathrm{R},\nu}^{\mathrm{K,K'}}(E,\mathbf{k}) \sigma_\nu^{\mathrm{K,K'}}(\mathbf{k}) + B_{\mathrm{R}}^{\mathrm{K,K'}}(E,\mathbf{k}) \right) g(E,\mathbf{k}) \,. \tag{B6}$$

The coefficients in the linear expression (B6) are defined by

$$A_{\mathrm{R},x}^{\mathrm{K,K'}}(E,\mathbf{k}) = \frac{1}{4}\left(\mathrm{Re}[(M_0^s(E,\mathbf{k}))^* M_{\pm2}^s(E,\mathbf{k})] - \mathrm{Re}[(M_0^p(E,\mathbf{k}))^* M_{\pm2}^p(E,\mathbf{k})] \right) \,, \tag{B7a}$$

$$A_{\mathrm{R},y}^{\mathrm{K,K'}}(E,\mathbf{k}) = \frac{1}{4}\left(\mathrm{Im}[(M_0^s(E,\mathbf{k}))^* M_{\pm2}^s(E,\mathbf{k})] - \mathrm{Re}[(M_0^p(E,\mathbf{k}))^* M_{\pm2}^p(E,\mathbf{k})] \right) \,, \tag{B7b}$$

$$A_{\mathrm{R},z}^{\mathrm{K,K'}}(E,\mathbf{k}) = \frac{1}{8}\left(|M_{\pm2}^s(E,\mathbf{k}))|^2 + |M_0^p(E,\mathbf{k}))|^2 - |M_0^s(E,\mathbf{k}))|^2 - |M_{\pm2}^p(E,\mathbf{k}))|^2 \right) \,, \tag{B7c}$$

and

$$B_{\mathrm{R}}^{\mathrm{K,K'}}(E,\mathbf{k}) = \frac{1}{8}\left(|M_0^s(E,\mathbf{k}))|^2 + |M_{\pm 2}^s(E,\mathbf{k}))|^2 - |M_0^p(E,\mathbf{k}))|^2 - |M_{\pm 2}^p(E,\mathbf{k}))|^2\right) . \tag{B8}$$

Finally, we express the imaginary part of the Fourier signal as

$$\mathrm{Im}[I_2(E,\mathbf{k})] = \left(\sum_{\nu=1,2,3} A_{\mathrm{I},\nu}^{\mathrm{K,K'}}(E,\mathbf{k})\sigma_\nu^{\mathrm{K,K'}}(\mathbf{k}) + B_{\mathrm{I}}^{\mathrm{K,K'}}(E,\mathbf{k})\right) g(E,\mathbf{k}) . \tag{B9}$$

The terms in Eq. (B9) are defined by

$$A_{\mathrm{I},x}^{\mathrm{K,K'}}(E,\mathbf{k}) = -\frac{1}{4}\left(\mathrm{Re}[(M_0^s(E,\mathbf{k}))^* M_{\pm 2}^p(E,\mathbf{k})] + \mathrm{Re}[(M_{\pm 2}^s(E,\mathbf{k}))^* M_0^p(E,\mathbf{k})]\right) , \tag{B10a}$$

$$A_{\mathrm{I},y}^{\mathrm{K,K'}}(E,\mathbf{k}) = -\frac{1}{4}\left(\mathrm{Im}[(M_0^s(E,\mathbf{k}))^* M_{\pm 2}^p(E,\mathbf{k})] - \mathrm{Im}[(M_{\pm 2}^s(E,\mathbf{k}))^* M_0^p(E,\mathbf{k})]\right) , \tag{B10b}$$

$$A_{\mathrm{I},z}^{\mathrm{K,K'}}(E,\mathbf{k}) = -\frac{1}{4}\left(\mathrm{Re}[(M_{\pm 2}^s(E,\mathbf{k}))^* M_{\pm 2}^p(E,\mathbf{k})] - \mathrm{Re}[(M_0^s(E,\mathbf{k}))^* M_0^p(E,\mathbf{k})]\right) , \tag{B10c}$$

and

$$B_{\mathrm{I}}^{\mathrm{K,K'}}(E,\mathbf{k}) = -\frac{1}{4}\left(\mathrm{Re}[(M_0^s(E,\mathbf{k}))^* M_0^p(E,\mathbf{k})] + \mathrm{Re}[(M_{\pm 2}^s(E,\mathbf{k}))^* M_{\pm 2}^p(E,\mathbf{k})]\right) . \tag{B11}$$

Summarizing Eqs. (B3)–(B11), we can express the three quantities $I_{\mathrm{CD}}(E,\mathbf{k})$, $\mathrm{Re}[I_2(E,\mathbf{k})]$, and $\mathrm{Im}[I_2(E,\mathbf{k})]$ as linear function of the pseudospin, which can conveniently be cast into the system of equations

$$\begin{bmatrix} I_{\mathrm{CD}}(E,\mathbf{k}) \\ \mathrm{Re}[I_2(E,\mathbf{k})] \\ \mathrm{Im}[I_2(E,\mathbf{k})] \end{bmatrix} = \begin{bmatrix} \mathcal{A}_{\mathrm{CD},x}^{\mathrm{K,K'}}(E,\mathbf{k}) & \mathcal{A}_{\mathrm{CD},y}^{\mathrm{K,K'}}(E,\mathbf{k}) & \mathcal{A}_{\mathrm{CD},z}^{\mathrm{K,K'}}(E,\mathbf{k}) \\ \mathcal{A}_{\mathrm{R},x}^{\mathrm{K,K'}}(E,\mathbf{k}) & \mathcal{A}_{\mathrm{R},y}^{\mathrm{K,K'}}(E,\mathbf{k}) & \mathcal{A}_{\mathrm{R},z}^{\mathrm{K,K'}}(E,\mathbf{k}) \\ \mathcal{A}_{\mathrm{I},x}^{\mathrm{K,K'}}(E,\mathbf{k}) & \mathcal{A}_{\mathrm{I},y}^{\mathrm{K,K'}}(E,\mathbf{k}) & \mathcal{A}_{\mathrm{I},z}^{\mathrm{K,K'}}(E,\mathbf{k}) \end{bmatrix} \begin{bmatrix} \sigma_x^{\mathrm{K,K'}}(\mathbf{k}) \\ \sigma_y^{\mathrm{K,K'}}(\mathbf{k}) \\ \sigma_z^{\mathrm{K,K'}}(\mathbf{k}) \end{bmatrix} + \begin{bmatrix} \mathcal{B}_{\mathrm{CD}}^{\mathrm{K,K'}}(E,\mathbf{k}) \\ \mathcal{B}_{\mathrm{R}}^{\mathrm{K,K'}}(E,\mathbf{k}) \\ \mathcal{B}_{\mathrm{I}}^{\mathrm{K,K'}}(E,\mathbf{k}) \end{bmatrix} , \tag{B12}$$

where we have abbreviated $\mathcal{A}_{r,\nu}^{\mathrm{K,K'}}(E,\mathbf{k}) = g(E,\mathbf{k})A_{r,\nu}^{\mathrm{K,K'}}(E,\mathbf{k})$ and $\mathcal{B}_r^{\mathrm{K,K'}}(E,\mathbf{k}) = g(E,\mathbf{k})B_r^{\mathrm{K,K'}}(E,\mathbf{k})$ ($r = \mathrm{CD,R,I}$).

To construct the coefficient matrix $\mathcal{A}_{r,\nu}^{\mathrm{K,K'}}(E,\mathbf{k})$ and the source term $\mathcal{B}_r^{\mathrm{K,K'}}(E,\mathbf{k})$ only two ingredients are required: (i) the atomic matrix elements (A2), and (ii) the energy conservation $g(E,\mathbf{k})$. The atomic matrix elements are mostly determined by the orbital symmetry (angular momentum), which can be guessed from the crystal structure or obtained from first principles. The energy conservation factor $g(E,\mathbf{k})$ can be extracted from experimental spectra by fitting a Gaussian function as function of E at every momentum point $\mathbf{k}$.

With all terms (except of the pseudospin vector) on the right-hand side of Eq. (B12) determined, Eq. (B12) can be solved for $\sigma_\nu^{\mathrm{K,K'}}(\mathbf{k})$. For a fixed energy E this is possible for all $\mathbf{k}$ with sufficient signal. The determinant of the coefficient matrix $\mathcal{A}_{r,\nu}^{\mathrm{K,K'}}(E,\mathbf{k})$ is proportional to $g(E,\mathbf{k})$; thus we solve Eq. (B12) only momenta obeying $g(E,\mathbf{k}) > \epsilon$. Normalizing $g(E,\mathbf{k})$ to one, we fix $\epsilon = 10^{-1}$.

We have tested the self-consistency within the theory by calculating the left-hand side of Eq. (B12) and solving for the pseudospin. Comparing the thus obtained solution to the directly calculated pseudospin (via Eq. (B1)) yields perfect agreement. We repeated the procedure adding small random noise to input signal; the reconstructed pseudospin is still in excellent agreement with the calculated texture.

For reconstructing the pseudospin from experimental data – as presented in the main text – a direct solution of Eq. (B12) in terms of matrix inversion gives rise to artifacts; most importantly, the normalization of the pseudospin

$$\sigma_x^{\mathrm{K,K'}}(\mathbf{k})^2 + \sigma_y^{\mathrm{K,K'}}(\mathbf{k})^2 + \sigma_z^{\mathrm{K,K'}}(\mathbf{k})^2 = 1 \tag{B13}$$

is violated. Therefore, we switch to the more least-square fitting algorithm. Furthermore, we constrain the solution by the normalization condition (B13) by adding a penalty term, which is chosen to ensure Eq. (B13) is obeyed up to 10^{-3}. Following this procedure yields the pseudospin textures presented in the main text.